

Article

## Inter-Algorithm Relationships for the Estimation of the Fraction of Vegetation Cover Based on a Two Endmember Linear Mixture Model with the VI Constraint

Kenta Obata and Hiroki Yoshioka \*

Department of Information Science and Technology, Aichi Prefectural University, 1522-3 Kumabari, Nagakute, Aichi, 480-1198, Japan; E-Mail: kenta.obata@cis.aichi-pu.ac.jp

\* Author to whom correspondence should be addressed; E-Mail: yoshioka@ist.aichi-pu.ac.jp; Tel.: +81-0561-64-1111, ext. 3302.

Received: 30 April 2010; in revised form: 29 June 2010 / Accepted: 29 June 2010 /

Published: 2 July 2010

---

**Abstract:** Measurements of the fraction of vegetation cover (FVC), retrieved from remotely sensed reflectance spectra, serves as a useful measure of land cover changes on the regional and global scales. A linear mixture model (LMM) is frequently employed to analytically estimate the FVC using the spectral vegetation index (VI) as a constraint. Variations in the application of this algorithm arise due to differences in the choice of endmember spectra and VI model assumptions. As a result, the retrieved FVCs from a single spectrum depend on those choices. Therefore, the mechanism underlying this dependency must be understood fully to improve the interpretation of the results. The objective of this study is to clarify the relationships among algorithms based on the LMM. The relationships were derived analytically by limiting both the number of endmembers and the spectral wavelength band to two each. Numerical experiments were conducted to demonstrate and validate the derived relationships. It was found that the relationships between two algorithms of this kind could be characterized by a single parameter that was determined by the endmember spectra and the coefficients of a VI model equation used in the algorithms.

**Keywords:** fraction of vegetation cover (FVC); linear mixture model (LMM); inter-algorithm relationship; vegetation index (VI); VI-isoline

---

## 1. Introduction

Information about the spatial and temporal distributions of vegetation plays an important role in several environmental studies fields, from local applications such as land-cover change to global climate change [1,2]. Changes in the quantity of vegetation cover directly affect water and energy budgets through plant transpiration, surface albedo, emissivity, and roughness [3]. Biophysical parameters retrieved from satellite observations are thus particularly important for improving our understanding of climatic, hydrologic, and geochemical cycles [4]. Satellite remote sensing is an effective and practical approach to facilitating such a broad range of environmental studies; it provides a retrospective and synoptic view of large areas, offering the opportunity to monitor the spatio-temporal dynamics of vegetation cover [5,6]. Vegetation quantity is often parameterized by the fractional area covered by green vegetation (horizontal density) and the leaf area index (vertical density) estimated from spectral reflectance measurements of satellite sensors [7]. In this study, we focus on a parameter that represents the horizontal density, called the fraction of vegetation cover (FVC) [8], which has been widely used for global and local analysis [8–12].

The algorithms for FVC retrieval fall into three categories based on the level of dependency on numerical techniques: (1) algorithms based on an analytical formula [13,14], in which the numerical process appear mainly in the determination of endmember spectra, distance measurement, and the minimization of the cost function; (2) algorithms based on numerical model inversion of the canopy radiative transfer [15–17]; and (3) algorithms using artificial intelligence, such as neural networks [18,19]. The user can choose an algorithm based on their needs, objectives, and the availability of external data sources. At the same time, algorithm variability implies that a value of the FVC retrieved from a single spectrum may vary according to the algorithm applied. Furthermore, because each category can be divided into several subcategories by considering the differences in assumptions and type of model used, the retrieved FVC values can vary even within a category. Thus, before we discuss the relationships among the three categories, relationships among algorithms within a category should be described. The purpose of this study is to examine the algorithms of the first category listed above to identify the source of variations in calculated FVC.

Our discussion is limited to the first category of FVC retrieval algorithms, although members of this category share several algorithmic variations and assumption of the linear mixture model (LMM). In these algorithms, FVC is modeled using the weights of the representative spectra, known as endmembers. Because of its simplicity, LMMs with very few endmembers have been used frequently over the years [5,7,13,14,20–30].

LMM-based retrieval algorithms can be characterized by the function and/or conditions under which the model is minimized [31]. In general, a set of weights is calculated that minimize differences between a modeled spectrum and the measured target pixel spectrum. Variations in the algorithm arise from the choice of variable used to measure the similarity between the model and the measurement data. For example, when reflectance is directly used as a variable, the minimization process considers the difference (often defined as the root mean square error, RMSE) between the modeled and measured spectrum [8–14,21,22,24,28,31–35]. Altering the reflectance into a spectral vegetation index (VI) produces another group of algorithms [1,4,7,25,26,36–39]. In this group, several conditions and

constraints are imposed to uniquely determine the set of weights. Therefore, the algorithms are further divided into several groups within this category.

If the values of the FVC derived by the two algorithms had a one-to-one relationship, one would not need to compute both algorithms. If the relationship is not one-to-one, one would always encounter some degree of uncertainty in estimating the FVC using different algorithms. If this is the case, this uncertainty is inherent in the algorithms, meaning that the uncertainty is unavoidable.

The objective of this paper is to investigate the relationships between FVC values calculated using the various algorithms in the context of the well-known LMM. This work elucidates the underlying causes of variation observed among results derived from different algorithms. We approach this problem analytically by limiting both the number of endmembers and the number of wavelength bands to two each. The simplicity enables us to treat the derivation analytically such that the conclusion is derived deterministically.

## 2. Model Assumptions and Retrieval Algorithms

This paper focuses on the LMM-based retrieval algorithms in which algorithmic variations arise mainly from the choice of endmember variable and the constraints imposed on the model. We consider two choices for the endmember variables, the measured reflectance and the VI obtained by band algebra. The constraints imposed on the model comprise the same two choices (reflectance and VI). The model assumptions and algorithms considered in this study are explained in the following section.

### 2.1. Model Assumptions

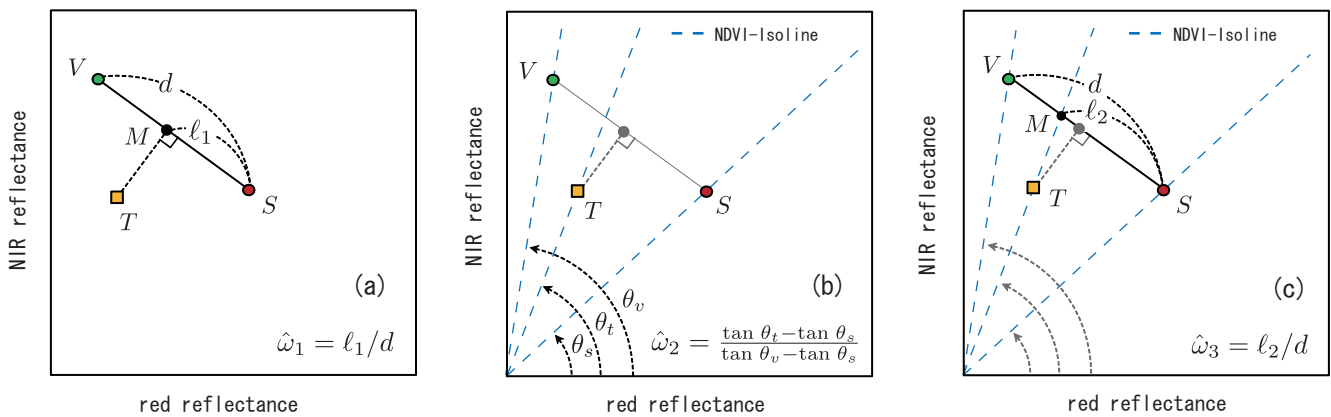
An LMM represents the spectrum from a target pixel as a linear combination of the representative components (endmembers) of the land surface. The weights of each endmember are the fractional area covered by the surface type. Two types of endmember, vegetation and non-vegetation, are assumed in this study. Under this assumption, the weight of the vegetation endmember corresponds to the fraction of vegetation cover (FVC). The spectra of vegetation and non-vegetation endmembers are represented by the vectors,  $\rho_v$  and  $\rho_s$ , respectively. The subscripts  $v$  and  $s$  denote vegetation or soil. Because the number of endmembers is limited to two, two measured spectral bands are sufficient to determine the weights of each endmember. Red and NIR bands are the most commonly chosen bands for the purpose of estimating FVC, and will be assumed in this study. Under these assumptions, the two vectors of the endmember spectra consist of red and NIR reflectance,  $\rho_v = (\rho_{v,r}, \rho_{v,n})$  and  $\rho_s = (\rho_{s,r}, \rho_{s,n})$ , where the subscripts  $r$  and  $n$  indicate the red and NIR bands, respectively.

The spectrum of the target pixel is modeled by the weighted linear sum of all endmembers, where the weights,  $\hat{\omega}$ , are given as

$$\rho_m(\hat{\omega}) = \hat{\omega}\rho_v + (1 - \hat{\omega})\rho_s. \quad (1)$$

The subscript  $m$  denotes the modeled spectrum. In Equation (1), the unity constraint is assumed. Note that the parameter  $\hat{\omega}$  is explicitly written in  $\rho_m$  for clarity.

**Figure 1.** Illustration of the three algorithms in red-NIR reflectance space. (a) Reflectance based LMM, (b) VI based LMM (for the case of NDVI), and (c) VI-Isoline based LMM (also for the case of NDVI). The marks denoted by  $V$  and  $S$  represent endmember spectrum of vegetation and non-vegetation surfaces, respectively.  $T$  and  $M$  represent measured and modeled spectrum, respectively. The key variables (such as  $d$ ,  $\ell_i$  ( $i = 1, 2$ ), and  $\theta$ ) which determine FVC estimation are also shown in the figures.



2.2. Algorithm-1: Reflectance-Based LMM

The standard algorithm uses reflectance directly (no VI involved,) and imposes a condition on the difference between the model and target reflectances to determine the weights. The minimization is performed on the root mean square error (RMSE) calculated directly from the reflectance. Thus, the cost function is the distance between the target spectrum,  $\rho_t = (\rho_{t,r}, \rho_{t,n})$ , and modeled spectrum,  $\rho_m$ . The FVC estimation,  $\hat{\omega}$ , is determined to minimize the distance,

$$\hat{\omega} = \frac{(\rho_v - \rho_s) \cdot (\rho_t - \rho_s)}{(\rho_v - \rho_s) \cdot (\rho_v - \rho_s)} = g_1(\rho_t). \tag{2}$$

RMSE minimization also implies that given a measure of distance, the algorithm finds  $\hat{\omega}$  to calculate the best fit for the spectrum within the model subspace. The model subspace occupies one dimension and is spanned by the vegetation and non-vegetation endmember spectra, as illustrated in Figure 1(a). In the figure, the three spectra (indicated by  $V$ ,  $S$ , and  $T$  for vegetation, non-vegetation, and target spectra, respectively) are plotted in the red-NIR reflectance space with the best fit spectrum denoted by  $M$ . When the Euclidean norm is chosen, the distance is measured, along with the line perpendicular to the model subspace spanned by the spectrum of the vegetation endmember,  $V$ , and that of non-vegetation endmember,  $S$  (Figure 1(a)). The FVC value,  $\hat{\omega}$ , is then determined as the ratio of the distance ( $\ell_1$ ) between  $S$  and  $M$  to the distance ( $d$ ) between  $S$  and  $V$ .

The FVC value obtained by this algorithm is not the same as the one obtained by the algorithms that use VI as an additional condition, as explained in the following subsections.

### 2.3. Algorithm-2: VI-Based LMM

One variation of the FVC retrieval algorithm is introduced by the choice of the variable that will be linearly blended. One choice is to use the VI instead of the direct reflectance to model a mixed pixel. Although numerous variations of the two-band VI ( $v$ ) have been proposed, their forms can be represented by the function  $f$ ,

$$\begin{aligned} v &= f(\boldsymbol{\rho}) \\ &= \frac{p_1\rho_r + q_1\rho_n + r_1}{p_2\rho_r + q_2\rho_n + r_2}, \end{aligned} \quad (3)$$

where the coefficients  $p_i$ ,  $q_i$ , and  $r_i$  depend on the actual choice of VI. In this study, we chose six VIs, namely, the normalized difference vegetation index (NDVI) [40], difference vegetation index (DVI) [41], perpendicular vegetation index (PVI) [42], soil-adjusted vegetation index (SAVI) [43], transformed SAVI (TSAVI) [44,45], and enhanced VI-2 (EVI2) [46] (EVI2 is a two-band version of the original EVI [47]). The coefficients for the VIs are summarized in Table 1.

The function  $f$  can also be rewritten in the form

$$f(\boldsymbol{\rho}) = \frac{\mathbf{c}_1 \cdot \boldsymbol{\rho} + r_1}{\mathbf{c}_2 \cdot \boldsymbol{\rho} + r_2}, \quad (4)$$

where the two vectors represented by  $\mathbf{c}_i$  are defined by

$$\mathbf{c}_i = (p_i, q_i), \quad (i = 1, 2). \quad (5)$$

Using the above definitions, the remotely sensed spectrum of a target pixel  $\boldsymbol{\rho}_t$  are transformed into the VI ( $v_t$ ) by

$$v_t = f(\boldsymbol{\rho}_t). \quad (6)$$

We also define the VI values of each endmember spectrum,  $v_v$  and  $v_s$  for the vegetation and non-vegetation endmember spectra, by

$$v_v = f(\boldsymbol{\rho}_v), \quad (7)$$

$$v_s = f(\boldsymbol{\rho}_s). \quad (8)$$

The VI-based algorithm simply models VI value as the linear sum of  $v_v$  and  $v_s$  using the weight  $\hat{\omega}$ :

$$v_m(\hat{\omega}) = \hat{\omega}v_v + (1 - \hat{\omega})v_s, \quad (9)$$

where  $v_m$  represents a modeled VI value. The weight can be determined by imposing a condition such that the VI modeled by Equation (9) is equal to the measured VI,

$$v_m(\hat{\omega}) = v_t. \quad (10)$$

Equation (10) can be solved for  $\hat{\omega}$  to give

$$\hat{\omega} = \frac{v_t - v_s}{v_v - v_s}. \quad (11)$$

**Table 1.** Coefficients of two-band VIs ( $p_i$ ,  $q_i$  and  $r_i$ ) used in this study.

|       | $p_1$          | $q_1$       | $r_1$         | $p_2$ | $q_2$       | $r_2$                      |
|-------|----------------|-------------|---------------|-------|-------------|----------------------------|
| NDVI  | -1             | 1           | 0             | 1     | 1           | 0                          |
| DVI   | -1             | 1           | 0             | 0     | 0           | 1                          |
| PVI   | $-a^\dagger$   | 1           | $-b^\dagger$  | 0     | 0           | $(1 + a)^{1/2 \dagger}$    |
| SAVI  | $-1.5^*$       | $1.5^*$     | 0             | 1     | 1           | $0.5^*$                    |
| TSAVI | $-a^2 \dagger$ | $a^\dagger$ | $-ab^\dagger$ | 1     | $a^\dagger$ | $-ab + X(1 + a^2)^\dagger$ |
| EVI2  | -2.5           | 2.5         | 0             | 2.4   | 1           | 1                          |

\* We assumed that  $L = 0.5$ .

$\dagger$   $a$  and  $b$  represent the slope and intercept of a soil line. We also assumed that  $X = 0.08$  in this study.

We then define a function  $g_2$  to represent the above transformation from  $v_t$  to  $\hat{\omega}$ ,

$$g_2(v_t) = \frac{v_t - v_s}{v_v - v_s}, \tag{12}$$

to have the following general representation of the composite function

$$\hat{\omega} = g_2(v_t) = g_2(f(\rho_t)) = (g_2 \circ f)(\rho_t). \tag{13}$$

An interpretation of this algorithm is illustrated in Figure 1(b) for the case of NDVI. In the figure, an estimation of the FVC,  $\hat{\omega}$ , can be approximated as the ratio of the angle spanned by the VI isoline, which passes through the target spectrum (denoted by the point T in the figure) and the isoline of the non-vegetation endmembers ( $\theta_t - \theta_s$ ), to the angle spanned by the VI isolines of vegetation and non-vegetation endmembers ( $\theta_v - \theta_s$ ). The actual representation of  $\hat{\omega}$  for the choice of NDVI with these angles becomes

$$\hat{\omega} = \frac{\tan \theta_t - \tan \theta_s}{\tan \theta_v - \tan \theta_s}. \tag{14}$$

#### 2.4. Algorithm-3: VI-Isoline-Based LMM

The VI-Isoline-based algorithm models VI using the function  $f$  based on a spectrum modeled by the LMM,

$$v_m(\hat{\omega}) = f(\rho_m(\hat{\omega})), \tag{15}$$

where  $v_m$  represents the modeled VI.  $\rho_m$  represents the spectrum as a linear combination of vegetation and non-vegetation endmember spectra.  $\hat{\omega}$  is the weight (estimated FVC) of the vegetation endmember. We expand the right hand side of the above equation to give

$$v_m(\hat{\omega}) = \frac{\mathbf{c}_1 \cdot \rho_m(\hat{\omega}) + r_1}{\mathbf{c}_2 \cdot \rho_m(\hat{\omega}) + r_2} \tag{16}$$

$$= \frac{\hat{\omega} \mathbf{c}_1 \cdot (\rho_v - \rho_s) + \mathbf{c}_1 \cdot \rho_s + r_1}{\hat{\omega} \mathbf{c}_2 \cdot (\rho_v - \rho_s) + \mathbf{c}_2 \cdot \rho_s + r_2}. \tag{17}$$

The FVC is determined by imposing the condition used in the previous algorithm (VI-based LMM),

$$v_m(\hat{\omega}) = v_t. \quad (18)$$

The above equation can be solved for  $\hat{\omega}$ ,

$$\hat{\omega} = \frac{(\mathbf{c}_1 - v_t \mathbf{c}_2) \cdot \boldsymbol{\rho}_s + r_1 - v_s r_2}{(v_t \mathbf{c}_2 - \mathbf{c}_1) \cdot (\boldsymbol{\rho}_v - \boldsymbol{\rho}_s)}. \quad (19)$$

We define a function  $g_3$  to represent the above transformation from  $v_t$  to  $\hat{\omega}$  as

$$g_3(v_t) = \frac{(\mathbf{c}_1 - v_t \mathbf{c}_2) \cdot \boldsymbol{\rho}_s + r_1 - v_s r_2}{(v_t \mathbf{c}_2 - \mathbf{c}_1) \cdot (\boldsymbol{\rho}_v - \boldsymbol{\rho}_s)}. \quad (20)$$

Finally, we arrive at a general representation of the composite function,

$$\hat{\omega} = g_3(v_t) = (g_3 \circ f)(\boldsymbol{\rho}_t). \quad (21)$$

This algorithm is illustrated in Figure 1(c) for the case of NDVI. In the figure, the modeled spectrum (denoted by the point  $M$ ) is determined by the intersection of the model subspace and the single dimension spanned by the endmember spectra ( $V$  for the vegetation and  $S$  for the non-vegetation) and the VI-isoline, which passes through the target spectrum (the point  $T$  in the figure). The value of FVC ( $\hat{\omega}$ ) is determined as the ratio of the distance ( $\ell_2$ ) between  $S$  and  $M$  to the distance ( $d$ ) between  $S$  and  $V$ .

### 3. Relationships Among the Algorithms

In this section, we explain the relationships among the FVCs calculated by the different algorithms. If the relationship between two transformations is one-to-one (and onto), the FVC estimated by one algorithm can be transformed into the other uniquely (without uncertainty). When this is the case, the two algorithms can be considered equivalent. In contrast, if the relationship is not one-to-one then it is impossible to deterministically transfer results from one algorithm to the other. Some degree of uncertainty would remain in the transformation. This implies that a comparison of the FVC values retrieved by different algorithms may contain bias errors. In this section, we clarify the relationships among the three algorithms using the functions defined in the previous section. To discriminate the  $\hat{\omega}$  derived by the three algorithms, we denote the estimated FVC values by  $\hat{\omega}_1$ ,  $\hat{\omega}_2$ , and  $\hat{\omega}_3$  for algorithms 1, 2, and 3, respectively.

#### 3.1. Relationships Between Algorithm-1 and the Others

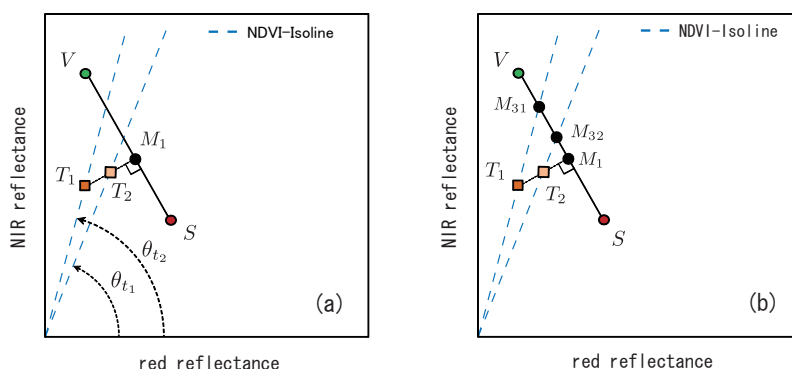
FVC estimation using algorithm-1,  $\hat{\omega}_1$ , can be obtained by the function  $g_1$  for a given target spectrum  $\boldsymbol{\rho}_t$  as

$$\hat{\omega}_1 = g_1(\boldsymbol{\rho}_t). \quad (22)$$

Although this transformation (from  $\boldsymbol{\rho}_t$  to  $\hat{\omega}_1$ ) maps  $\boldsymbol{\rho}_t$  uniquely to  $\hat{\omega}_1$ , the inverse transformation,  $g_1^{-1}$ , does not map  $\hat{\omega}_1$  uniquely to a single value of  $\boldsymbol{\rho}_t$ . We define a set of reflectance spectra that give  $\hat{\omega}_1$  as  $S_1(\hat{\omega}_1)$ :

$$S_1(\hat{\omega}_1) = \{\boldsymbol{\rho} \mid g_1(\boldsymbol{\rho}) = \hat{\omega}_1\}. \quad (23)$$

**Figure 2.** The relationship between the algorithm-1 and the other two in red-NIR reflectance space. (a) Relationship between algorithm-1 and algorithm-2, (b) algorithm-1 and algorithm-3.  $V$  and  $S$  represent endmember spectrum of vegetation and non-vegetation surface.  $T_1$  and  $T_2$  are target spectra.  $M_1$  is a modeled spectrum by algorithm-1 for two measured spectra denoted by  $T_1$  and  $T_2$ .  $M_{31}$  and  $M_{32}$  are modeled spectra by algorithm-3 for  $T_1$  and  $T_2$ , respectively. The figures illustrate the source of uncertainties between the algorithms.



A set of  $\hat{\omega}_2$  that can be mapped from  $\rho \in S_1(\hat{\omega}_1)$  is then defined by  $T_{1 \rightarrow 2}(\hat{\omega}_1)$  as

$$T_{1 \rightarrow 2}(\hat{\omega}_1) = \{\hat{\omega}_2 \mid \hat{\omega}_2 = (g_2 \circ f)(\rho), \rho \in S_1(\hat{\omega}_1)\}. \tag{24}$$

Similarly, the relationship between algorithm-1 and algorithm-3 can be represented by defining  $T_{1 \rightarrow 3}(\hat{\omega}_1)$  as

$$T_{1 \rightarrow 3}(\hat{\omega}_1) = \{\hat{\omega}_3 \mid \hat{\omega}_3 = (g_3 \circ f)(\rho), \rho \in S_1(\hat{\omega}_1)\}. \tag{25}$$

Since the mappings  $T_{1 \rightarrow 2}$  and  $T_{1 \rightarrow 3}$  are not one-to-one, the relationships between  $\hat{\omega}_1$  and the others ( $\hat{\omega}_2$  and  $\hat{\omega}_3$ ) are not uniquely determined. This implies some degree of uncertainty in the relationships between the two algorithms. This fact is clearly illustrated in Figure 2(a). The figure shows the geometrical relationship between algorithms-1 and -2 in the red-NIR reflectance space. In the figure, the spectra of the two endmembers are represented by the points denoted by  $V$  and  $S$ . The two target spectra represented by  $T_1$  and  $T_2$  produce an identical FVC value by algorithm-1 because the nearest point in the model subspace ( $M_1$ ) is the same for both  $T_1$  and  $T_2$ . However,  $\theta_{t_1}$  and  $\theta_{t_2}$  are not the same, which means that the values of  $\hat{\omega}_2$  for  $T_1$  and  $T_2$  are different. Similarly, the relationship between  $\hat{\omega}_1$  and  $\hat{\omega}_3$  is illustrated in Figure 2(b). Although the two target spectra  $T_1$  and  $T_2$  yield the same FVC value by algorithm-1, the FVCs retrieved by algorithm-3 are different (denoted by  $M_{31}$  and  $M_{32}$ ).

In summary, FVC retrieved by algorithm-1 is not uniquely transformed to a single value of FVC retrieved by algorithms-2 and -3. Non-uniqueness is a source of uncertainty induced by the choice of retrieval algorithm.

### 3.2. Relationship Between Algorithms-2 and -3

The relationship between these two algorithms is somewhat different from the relationships introduced in the previous subsection. Major difference arise from the fact that both algorithms use VI, although the implementation is not identical. FVC estimation by algorithm-2 can be obtained directly from the VI value of the target spectrum ( $v_t$ ) using the function  $g_2$ ,

$$\hat{\omega}_2 = g_2(v_t). \tag{26}$$

FVC estimation by algorithm-3,  $\hat{\omega}_3$ , can also be written as

$$\hat{\omega}_3 = g_3(v_t). \tag{27}$$

In the above two equations,  $v_t$  is a common variable that can be removed by combining the two equations. Solving Equation (26) for  $v_t$  using the inverse function of  $g_2$  gives

$$v_t = g_2^{-1}(\hat{\omega}_2), \tag{28}$$

then substituting Equation (28) into Equation (27) yields a relationship between  $\hat{\omega}_2$  and  $\hat{\omega}_3$  defined by the composite function

$$\hat{\omega}_3 = (g_3 \circ g_2^{-1})(\hat{\omega}_2). \tag{29}$$

Similarly,  $\hat{\omega}_2$  can be written as a function of  $\hat{\omega}_3$

$$\hat{\omega}_2 = (g_2 \circ g_3^{-1})(\hat{\omega}_3). \tag{30}$$

Because both  $g_2$  and  $g_3$  are one-to-one transformations, the composite functions in Equations (29) and (30) are also one-to-one transformations. Therefore, the FVC value estimated by one algorithm can be uniquely transformed to the other. The actual form of Equation (29) becomes

$$\hat{\omega}_3 = \frac{\hat{\omega}_2\phi_2 + \psi_2}{\hat{\omega}_2\phi_1 + \psi_1}, \tag{31}$$

where

$$\phi_1 = (v_v - v_s)\mathbf{c}_2 \cdot (\boldsymbol{\rho}_v - \boldsymbol{\rho}_s), \tag{32a}$$

$$\phi_2 = -(v_v - v_s)(\mathbf{c}_2 \cdot \boldsymbol{\rho}_s + r_2), \tag{32b}$$

$$\psi_1 = (v_s\mathbf{c}_2 - \mathbf{c}_1) \cdot (\boldsymbol{\rho}_v - \boldsymbol{\rho}_s), \tag{32c}$$

$$\psi_2 = (\mathbf{c}_1 - v_s\mathbf{c}_2) \cdot \boldsymbol{\rho}_s + r_1 - v_s r_2. \tag{32d}$$

Because  $(v_v - v_s)$  and  $(\mathbf{c}_2 \cdot \boldsymbol{\rho}_s + r_2)$  are positive,  $\phi_2$  is always negative,

$$\phi_2 < 0. \tag{33}$$

Furthermore, the following relationships can be found directly from the definitions

$$\phi_2 = \phi_1 + \psi_1, \tag{34}$$

$$\psi_2 = 0. \tag{35}$$

Using these relationships, Equation (31) can be rewritten with only one variable  $\nu$  as

$$\hat{\omega}_3 = \frac{\hat{\omega}_2}{\nu\hat{\omega}_2 + 1 - \nu}, \quad (36)$$

where

$$\nu = \frac{\phi_1}{\phi_1 + \psi_1}, \quad (37a)$$

$$1 - \nu = \frac{\psi_1}{\phi_1 + \psi_1}. \quad (37b)$$

Note that this relationship can be obtained if and only if the choice of VI in both algorithms-2 and -3 are equivalent. Thus,  $\nu$  depends on the choice of VI and endmember spectra of vegetation and non-vegetation class. The forms of the coefficients  $\phi_1$  and  $\psi_1$  for several VIs are summarized in Table 2.

When  $\nu$  becomes 0,  $\hat{\omega}_3$  is identical to  $\hat{\omega}_2$ , implying that it is not necessary to investigate the relationship between these variables in this particular case. This case occurs when the inner product of the vectors  $\mathbf{c}_2$  and  $\boldsymbol{\rho}_v - \boldsymbol{\rho}_s$  becomes 0 (the vectors are orthogonal).

For the discussion presented in this study, we consider the range of  $\nu$  based on the following inequality, which holds for all VIs in Table 2.

$$\mathbf{c}_2 \cdot \boldsymbol{\rho}_v > -r_2. \quad (38)$$

(Most likely, this inequality holds for the other two-band VIs represented by the general form in Equation (4)). Subtracting  $\mathbf{c}_2 \cdot \boldsymbol{\rho}_s$  from the both sides of the above inequality then multiplying by  $(v_v - v_s)$  yields

$$(v_v - v_s)\mathbf{c}_2 \cdot (\boldsymbol{\rho}_v - \boldsymbol{\rho}_s) > -(v_v - v_s)(\mathbf{c}_2 \cdot \boldsymbol{\rho}_s + r_2). \quad (39)$$

The left and right hand sides are the definitions of  $\phi_1$  and  $\phi_2$ , respectively. The inequality can also be written as

$$\phi_1 > \phi_2. \quad (40)$$

From Equation (34), the variable  $\nu$ , which is defined as the ratio of  $\phi_1$  to  $\phi_2$ , is less than one.

$$\nu < 1. \quad (41)$$

In the following discussion, the above range of values for  $\nu$  should be considered. We exclude the trivial case  $\nu = 0$  from the derivations in the following section. This approach will help us analyze the maximum difference between  $\hat{\omega}_2$  and  $\hat{\omega}_3$  provided in subsection 4.3. A detailed discussion of the difference in estimated FVC values is provided with the numerical examples in the next section.

**Table 2.** Summary of  $\phi_1$  and  $\psi_1$  for the VIs considered in this study.  $\rho_{v,r}$  and  $\rho_{v,n}$  are the red and NIR reflectance of vegetation endmember, respectively. Likewise,  $\rho_{s,r}$  and  $\rho_{s,n}$  are the red and NIR reflectance of non-vegetation endmember, respectively.  $a$  represents a slope of soil line.

|       | $\phi_1$  | $\psi_1$   |
|-------|---|--|
| NDVI  | $(v_v - v_s)(\rho_{v,r} + \rho_{v,n} - \rho_{s,r} - \rho_{s,n})$      | $(1 + v_s)(\rho_{v,r} - \rho_{s,r}) - (1 - v_s)(\rho_{v,n} - \rho_{s,n})$        |
| DVI   | 0   | $\rho_{v,r} - \rho_{v,n} - \rho_{s,r} + \rho_{s,n}$                              |
| PVI   | 0   | $a(\rho_{v,r} - \rho_{s,r}) - \rho_{v,n} + \rho_{s,n}$                           |
| SAVI  | $(v_v - v_s)(\rho_{v,r} + \rho_{v,n} - \rho_{s,r} - \rho_{s,n})$      | $(1.5 + v_s)(\rho_{v,r} - \rho_{s,r}) - (1.5 - v_s)(\rho_{v,n} - \rho_{s,n})$    |
| TSAVI | $(v_v - v_s)[\rho_{v,r} - \rho_{s,r} + a(\rho_{v,n} - \rho_{s,n})]$   | $(a^2 + v_s)(\rho_{v,r} - \rho_{s,r}) + a(v_s - 1)(\rho_{v,n} - \rho_{s,n})$     |
| EVI2  | $(v_v - v_s)[2.4(\rho_{v,r} - \rho_{s,r}) + \rho_{v,n} - \rho_{s,n}]$ | $(2.4v_s + 2.5)(\rho_{v,r} - \rho_{s,r}) + (v_s - 2.5)(\rho_{v,n} - \rho_{s,n})$ |

## 4. Numerical Results

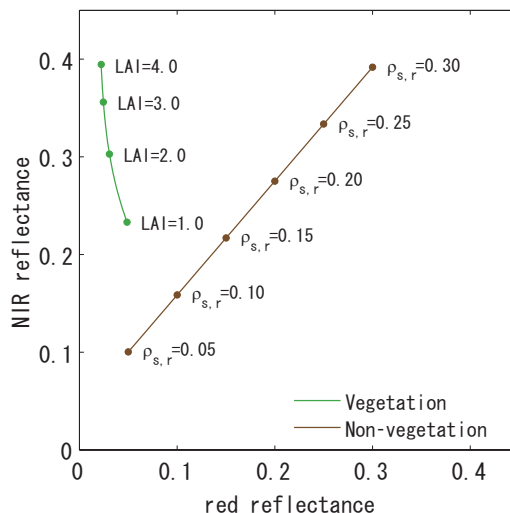
### 4.1. Uncertainties in the Relationships

Numerical experiments were conducted to demonstrate and validate the derived relationships between algorithm-1 and algorithms-2 and -3. We assumed that a target pixel could be divided into vegetated and non-vegetated (bare soil) surface cover. Thus, the reflectance spectra from the target pixel could be modeled by a two-endmember linear mixture model. The endmember spectrum of the vegetation class was parameterized as a function of the leaf area index (LAI) using a canopy radiative transfer model GeoSail [17]. For this simulation, soil reflectance beneath the canopy layer was assumed to be constant. The red reflectance of the soil layer within a canopy portion was fixed to 0.1, and the NIR reflectance of the soil surface was modeled to be 0.1586 by assuming a general soil line reported in [48]. The slope  $a$  and intercept  $b$  of the soil line were 1.166 and 0.042, respectively. The endmember spectrum of the bare soil portion of a target pixel was modeled by the same general soil line such that the soil endmember spectrum was parameterized by the soil reflectance of the red band ( $\rho_{r,s}$ ). The two sets of endmember spectra are plotted in Figure 3.

To demonstrate the relationships among the FVCs retrieved by the three algorithms, we prepared a set of reflectance spectra consisting of 388 pairs of red and NIR reflectance values, plotted in Figure 4(a). In the figure, the endmember spectra of the vegetation and non-vegetation classes are superimposed. These endmember spectra were obtained by assuming LAI= 4 and  $\rho_{r,s} = 0.15$  for vegetation and non-vegetation classes, respectively. (Note that reflectances of the NIR band for the non-vegetation endmember were obtained using the general soil line.) We chose NDVI as a representative VI for algorithms-2 and -3 in this subsection. The FVC values were computed using the three algorithms for all reflectance spectra shown in Figure 4(a).

The relationships among the retrieved FVC values using the three algorithms ( $\hat{\omega}_1$ ,  $\hat{\omega}_2$ , and  $\hat{\omega}_3$ ) are shown as cross plots of the three combinations of  $\hat{\omega}$  in Figures 4(b–d). The FVC values estimated by algorithm-1 were plotted against the values estimated by algorithms-2 and -3 in Figures 4(b) and (c), respectively. Figure 4(d) shows the relationships between algorithms-2 and -3. From these results, FVC

**Figure 3.** Plot of endmember spectra in red-NIR reflectance space. Sequences of vegetation and non-vegetation endmember are represented as a green and a brown line, respectively. Values of LAI and red reflectance of non-vegetation surface ( $\rho_{s,r}$ ) are indicated in the lines.



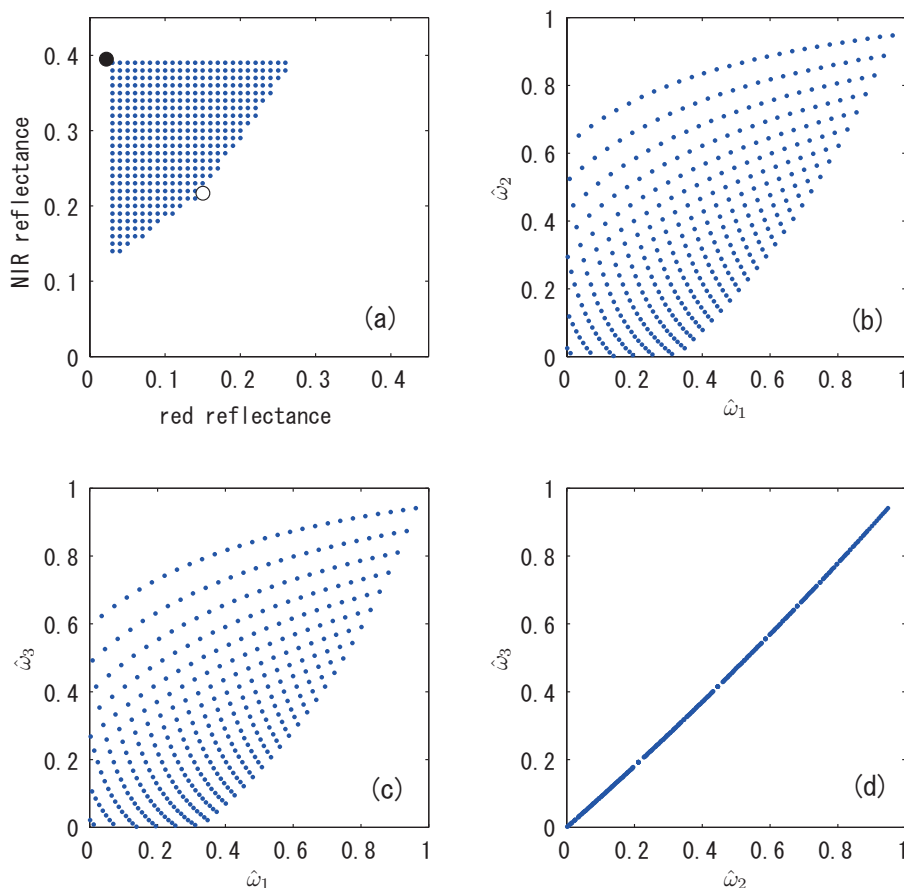
estimation by algorithm-1 was not transformed uniquely to a single FVC value by algorithms-2 and -3. In consequence, some degree of uncertainty is present in these algorithms. The uncertainty is inherent in any comparison between these two estimations. In contrast, a one-to-one relationship exists between algorithms-2 and -3 (Figure 4(d)). This result clearly validated the one-to-one relationship derived between algorithms-2 and -3. The FVC estimation by either algorithm can be transformed uniquely to the other (thus, the two algorithms can be considered equivalent.)

#### 4.2. Differences Between $\hat{\omega}_2$ and $\hat{\omega}_3$ as a Function of Endmember Spectra

The previous subsection demonstrated that the difference between the results of algorithms-2 and -3 appeared to depend on the FVC value, although the relationship was one-to-one between the two algorithms. In fact, the difference also depended on the endmember spectra and the choice of VI (which will be confirmed in the next subsection.) In the following subsections, we will investigate these differences thoroughly.

The difference between  $\hat{\omega}_2$  and  $\hat{\omega}_3$  was obtained using several endmember spectra for both non-vegetation (soil) and vegetation classes with four different VIs (NDVI, SAVI, TSAVI, and EVI2) shown in Figures 5(a–d) and 6(a–d). We excluded DVI and PVI from the analysis because  $\phi_1 = 0$  for these VIs (meaning that there is no difference between  $\hat{\omega}_2$  and  $\hat{\omega}_3$ .) Figures 5(a–d) show the plots of  $(\hat{\omega}_2 - \hat{\omega}_3)$  at a fixed vegetation endmember spectrum simulated by setting LAI to 4 (the endmember spectrum is shown in Figure 3). Thus, the variations arose only from the choice of soil endmember spectrum (the variations of which are shown in Figure 3). Figures 5(a–d) clearly show that the difference  $(\hat{\omega}_2 - \hat{\omega}_3)$  depended on the choice of soil endmember spectrum assumed for the FVC retrieval. Similarly, Figures 6(a–d) show the dependency of  $(\hat{\omega}_2 - \hat{\omega}_3)$  on the choice of vegetation endmember spectrum. The soil endmember spectrum was fixed for Figures 6(a–d) at  $\rho_s = (0.15, 0.22)$ . These results indicated the dependency of the FVC estimation difference on the vegetation endmember spectrum. In addition,

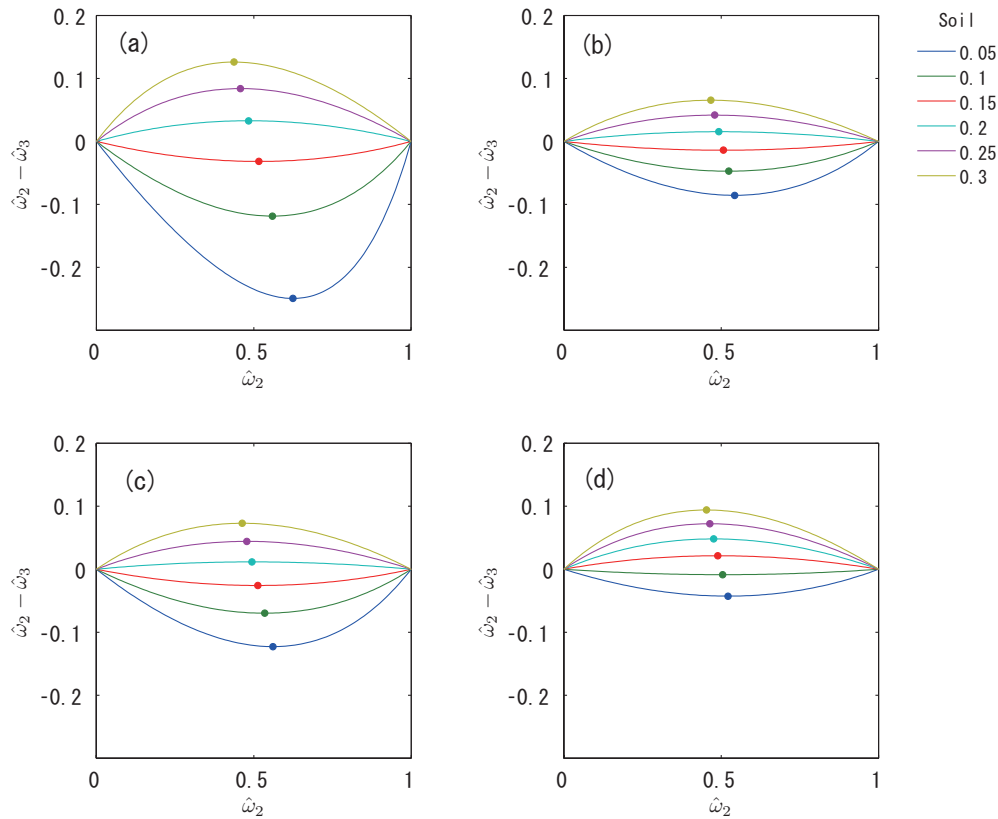
**Figure 4.** Hypothetical target spectra in red-NIR reflectance space and cross plots of FVC estimations by the three algorithms for the target spectra. (a) Scatter plot of target spectra (dot), endmember spectra of vegetation (filled circle) and non-vegetation (empty circle) in red-NIR reflectance space. (b) Cross plots of  $\hat{\omega}_2$  and  $\hat{\omega}_1$ , (c)  $\hat{\omega}_3$  and  $\hat{\omega}_1$ , and (d)  $\hat{\omega}_3$  and  $\hat{\omega}_2$ .



Figures 5(a–d) and 6(a–d) implied the following facts: (1) The differences could be both positive and negative (depending on the choice of endmember); however, the signature of the difference remained the same once the endmember spectra were fixed. (2) The maximum differences and the point of  $\hat{\omega}_2$  where the maximum occurred also depended on the choice of endmember (the maximum did not occur at the same value of  $\hat{\omega}_2$ .) (3) The relationships between algorithms-2 and -3 showed some degree of nonlinearity (depending on the endmember spectra.)

To demonstrate the effects of both endmember spectra simultaneously, the difference ( $\hat{\omega}_2 - \hat{\omega}_3$ ) was plotted for several values of  $\hat{\omega}_2$  (0.2, 0.5, and 0.8) as a function of LAI (as a parameter for the vegetation endmember spectrum) and red reflectance of the soil endmember (Figures 7(a-1)). From these results, the influence of the soil endmember spectrum was large relative to that of the vegetation endmember for all VIs. (As a result, the isolines in Figure 7 were nearly horizontal.) This implied that differences in soil brightness may induce discrepancies in the FVCs retrieved by the two algorithms that are larger than the differences produced by the choice of vegetation endmember spectrum.

**Figure 5.** Plot of  $(\hat{\omega}_3 - \hat{\omega}_2)$  against  $\hat{\omega}_2$  under various non-vegetation endmember spectra for the case of four VIs ((a) NDVI, (b) SAVI, (c) TSAVI, and (d) EVI2). The endmember spectrum of vegetation class is fixed at  $\rho_v = (0.02, 0.40)$  corresponding to the value of LAI= 4. The maximum difference for each case is indicated by a dot (computed from Equations (46) and (47)).



### 4.3. The Maximum Difference Between $\hat{\omega}_2$ and $\hat{\omega}_3$

As mentioned in the previous subsection, the maximum difference occurred at somewhat different values of  $\hat{\omega}_2$  (Figures 5 and 6) depending on the choice of endmember spectra. Additionally, the sign and absolute value of the difference depended on the endmember spectra. In this subsection, we will investigate this point.

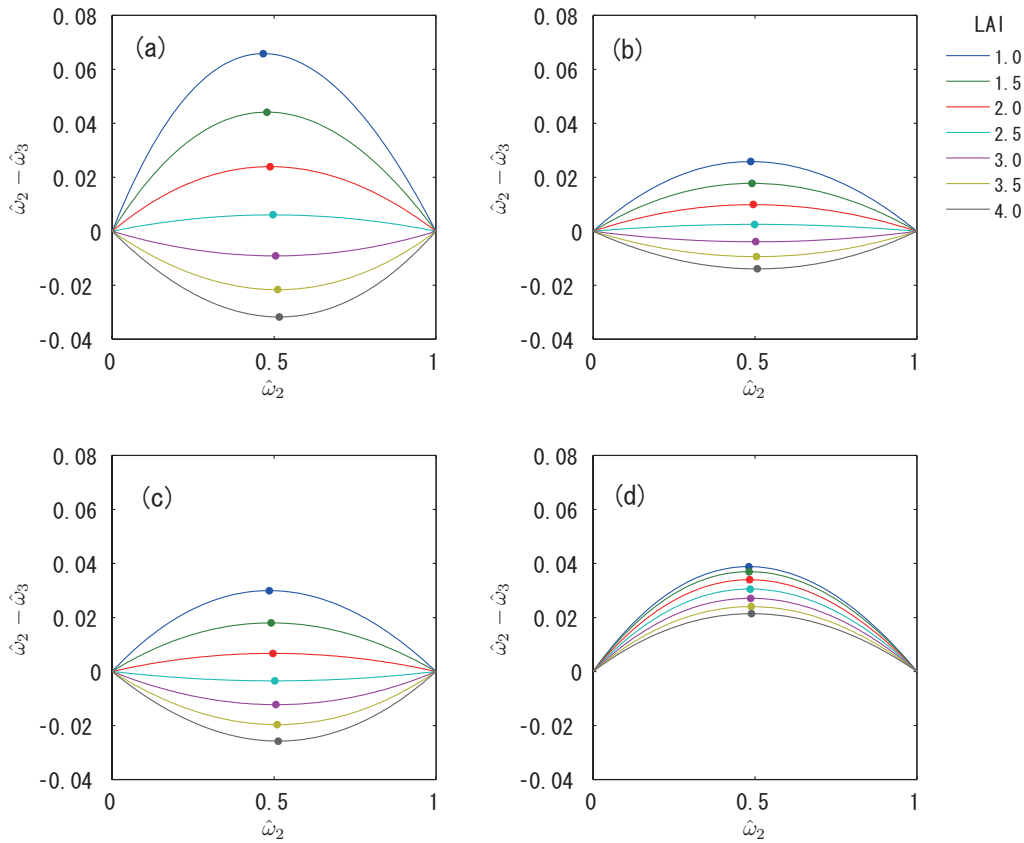
We first rewrite the difference between  $\hat{\omega}_2$  and  $\hat{\omega}_3$  (denoted as the function  $h$ ) in terms of  $\hat{\omega}_2$  and  $\nu$ :

$$\begin{aligned}
 h(\hat{\omega}_2) &= \hat{\omega}_3 - \hat{\omega}_2 \\
 &= \frac{-\nu\hat{\omega}_2(\hat{\omega}_2 - 1)}{\nu\hat{\omega}_2 + 1 - \nu}.
 \end{aligned}
 \tag{42}$$

To derive the value of  $\hat{\omega}_2$  at which the maximum of  $h(\hat{\omega}_2)$  occurs (defined as  $\hat{\omega}_{2max}$ ), we consider the partial derivative of the function  $h$  with respect to  $\hat{\omega}_2$

$$\frac{\partial h(\hat{\omega}_2)}{\partial \hat{\omega}_2} = \frac{\nu^2\hat{\omega}_2^2 + 2\nu(1 - \nu)\hat{\omega}_2 - \nu(1 - \nu)}{(\nu\hat{\omega}_2 + 1 - \nu)^2}.
 \tag{43}$$

**Figure 6.** Plot of  $(\hat{\omega}_3 - \hat{\omega}_2)$  against  $\hat{\omega}_2$  under various vegetation endmember spectra for the case of four VIs ((a) NDVI, (b) SAVI, (c) TSAVI, and (d) EVI2). The endmember spectrum of non-vegetation class is fixed at  $\rho_s = (0.15, 0.22)$ . The maximum difference for each case is indicated by a dot (computed from Equations (46) and (47)).



The maximum of  $h$  occurs at the root of the partial derivative. Because the denominator is always positive,  $\hat{\omega}_{2max}$  should satisfy the following relationship:

$$\nu\hat{\omega}_{2max}^2 + 2\nu(1 - \nu)\hat{\omega}_{2max} - \nu(1 - \nu) = 0. \tag{44}$$

Solving for  $\hat{\omega}_{2max}$ , we have

$$\hat{\omega}_{2max} = \frac{\nu - 1 \pm \sqrt{1 - \nu}}{\nu}. \tag{45}$$

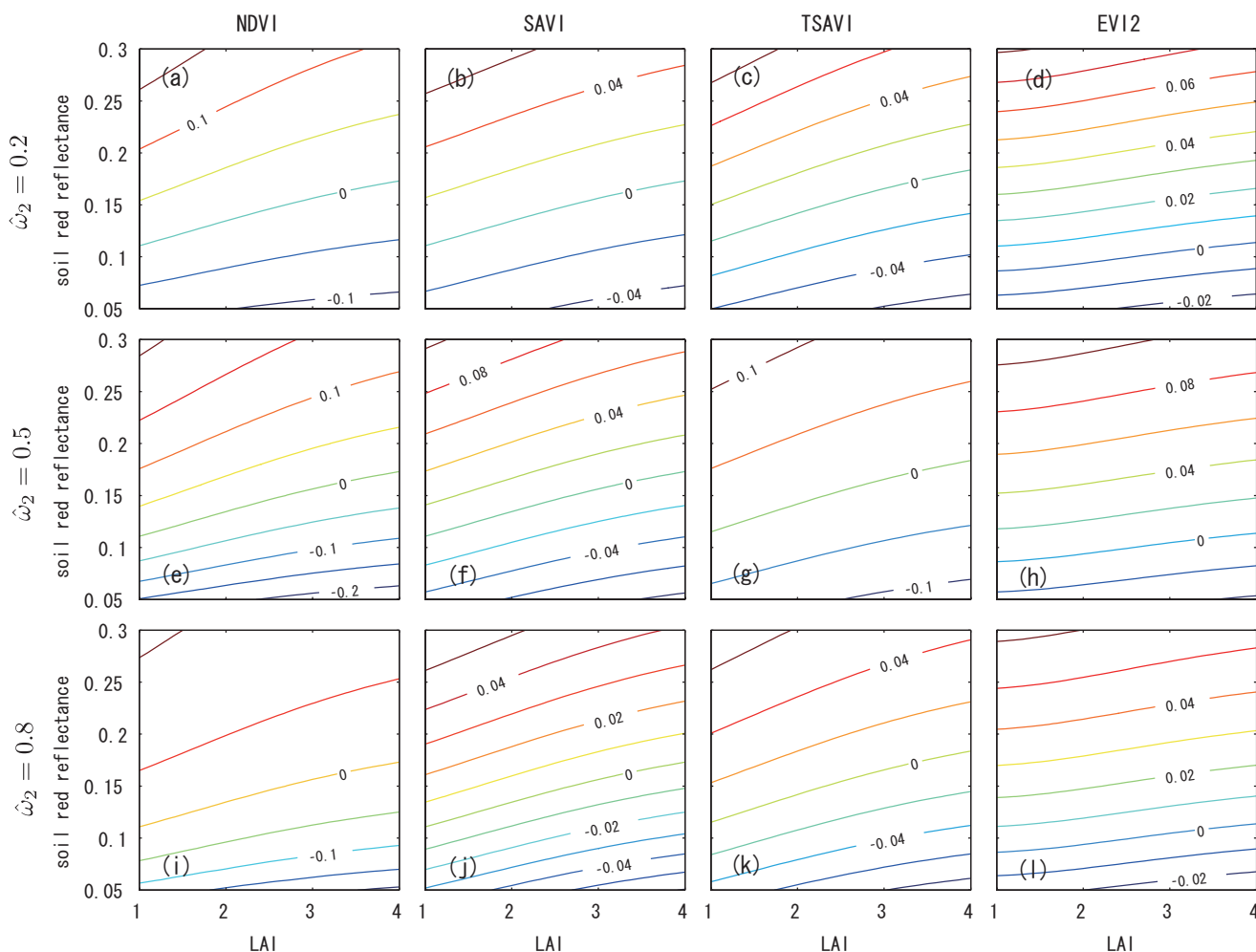
Although two values will satisfy Equation (44), only the positive value is an appropriate choice for the following reason. When  $0 < \nu < 1$ , the value of  $\hat{\omega}_{2max}$  exceeds one when the negative sign is chosen. Thus, the positive sign is the only choice that yields an appropriate value ( $\hat{\omega}_{2max}$  becomes smaller than 1.0 for this case):

$$\hat{\omega}_{2max} = \frac{\nu - 1 + \sqrt{1 - \nu}}{\nu}. \tag{46}$$

Likewise, when  $\nu < 0$ , the positive value should be chosen because  $(\nu - 1)/\nu > 1$  and  $\sqrt{1 - \nu}/\nu < 0$ . The maximum difference can be obtained by substituting  $\hat{\omega}_{2max}$  into Equation (42) to obtain

$$h(\hat{\omega}_{2max}) = \frac{(\sqrt{1 - \nu} - 1)^2}{\nu}. \tag{47}$$

**Figure 7.** Contour plots of  $(\hat{\omega}_3 - \hat{\omega}_2)$  for the cases of (a) NDVI, (b) SAVI, (c) TSAVI, and (d) EVI2 as a function of vegetation and non-vegetation endmember spectra at fixed values of  $\hat{\omega}_2$  (0.2, 0.5 and 0.8.) Variations of vegetation and non-vegetation endmember spectra are represented by LAI (in x-axis) and soil reflectance of red band (in y-axis), respectively.



Equation (47) suggests that the sign of  $h(\hat{\omega}_2)$  can be determined from the sign of  $\nu$ . When  $\nu$  is positive,  $\hat{\omega}_3$  is larger than  $\hat{\omega}_2$ .

#### 4.4. Variations of $\nu$ , $\phi_1$ , $\psi_1$ , and $h(\hat{\omega}_{2max})$ with Variations in the Endmember Spectra

The relationship between algorithms-2 and -3 can be represented as a function of a single variable ( $\nu$ ), as described in subsections 4.2 and 4.3. In this subsection, we focus on the behavior of  $\nu$  and its influence on the sign of  $(\hat{\omega}_3 - \hat{\omega}_2)$ , its magnitude, and  $\hat{\omega}_{2max}$ . Note that because  $\nu$  is defined by  $\phi_1$  and  $\psi_1$  (and the sum of these two,  $\phi_2$ ), we need to examine their variations as a function of endmember spectra.

Figures 8(a–t) summarize the contour plots of  $\phi_1$ ,  $\psi_1$ ,  $\phi_2$ ,  $\nu$ , and  $1 - \nu$  as a function of vegetation endmember spectrum (represented by LAI in the x-axis) and non-vegetation endmember spectrum

**Figure 8.** Variations of  $\phi_1, \psi_1, \phi_2, \nu,$  and  $1 - \nu$  as a function of vegetation and non-vegetation endmember spectra represented by LAI and soil red reflectance, respectively. The plots are arranged in a matrix form, where the choice of VI is arranged column-wise, and the five coefficients are arranged row-wise.

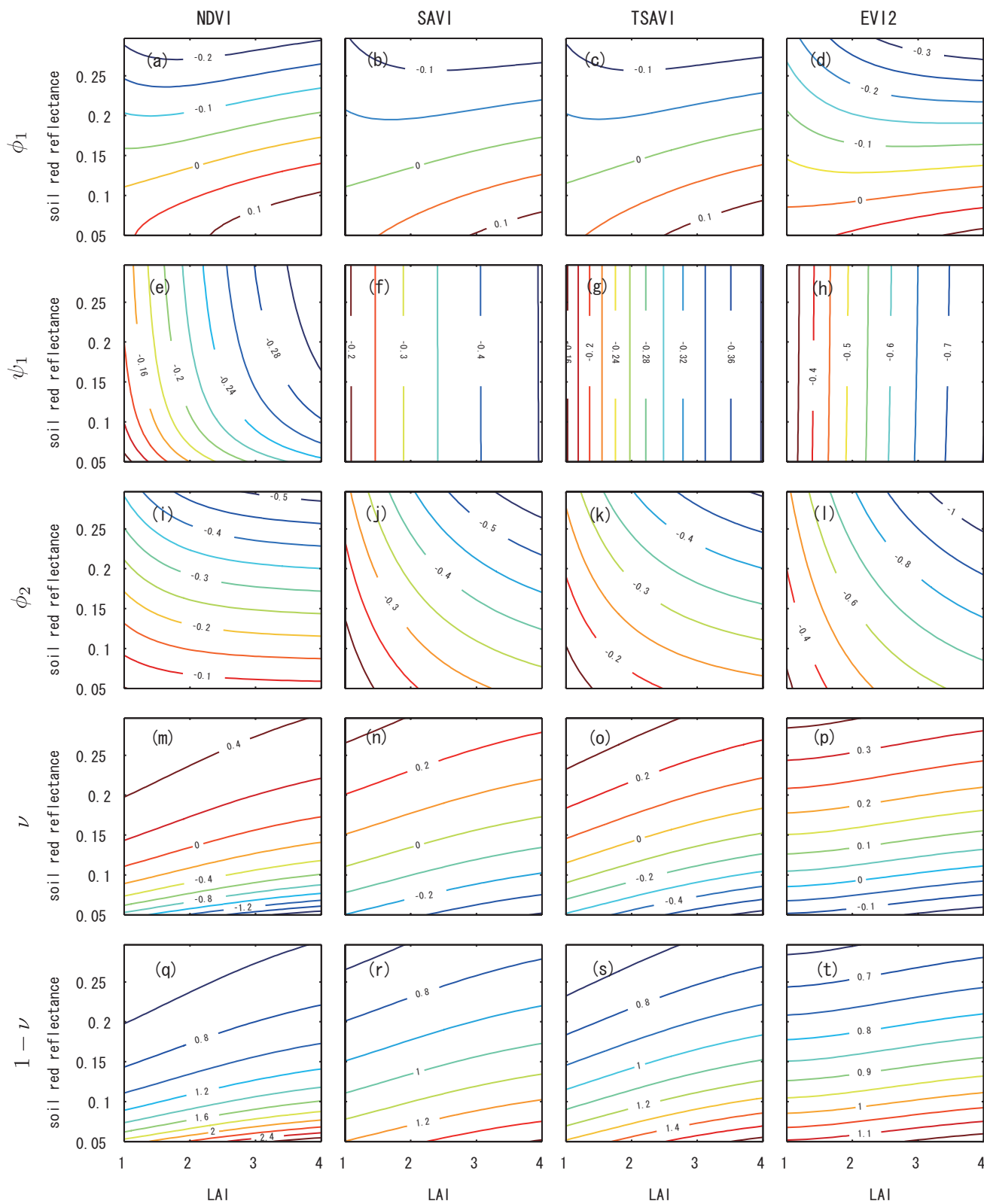
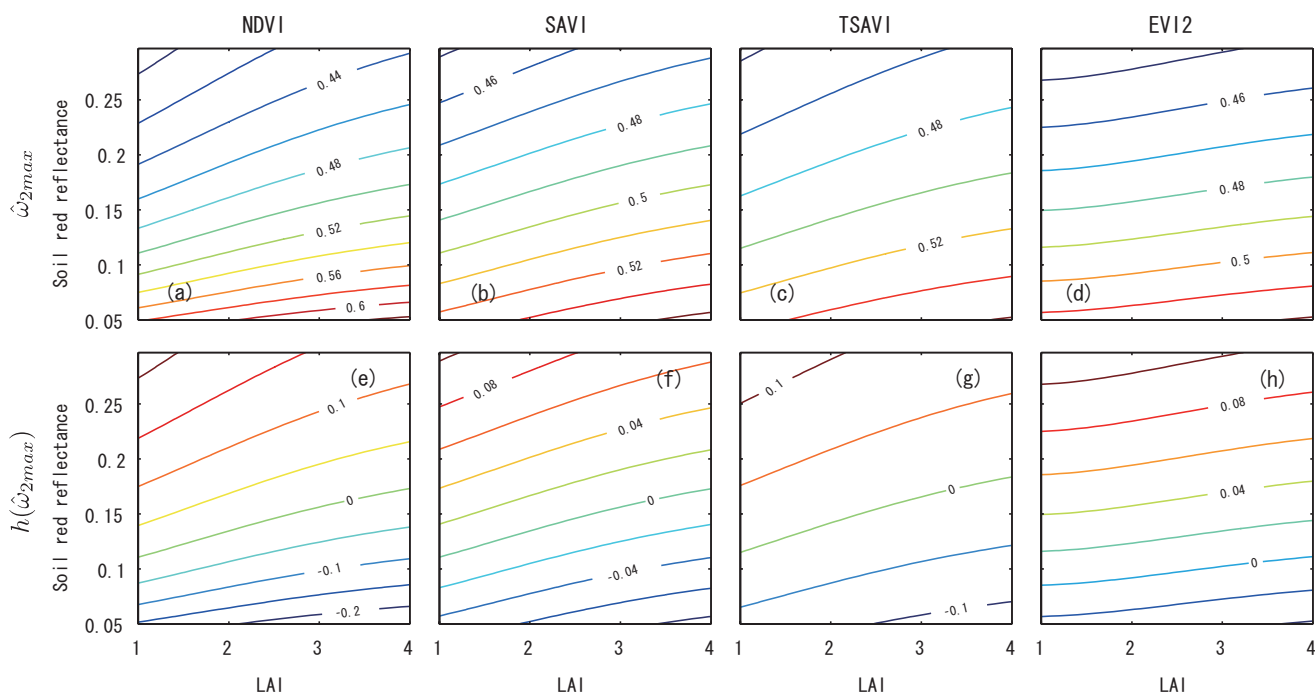


**Figure 9.** Variations of  $\hat{\omega}_{2max}$  and  $h(\hat{\omega}_{2max})$  as a function of spectrum of vegetation and non-vegetation endmember. The upper figures (a)-(d) are the results of  $\hat{\omega}_{2max}$  for the case of NDVI, SAVI, TSAVI and EVI2 (arranged column-wise), respectively. The lower figures (e)-(h) are the results of  $h(\hat{\omega}_{2max})$ .



(represented by soil reflectance of the red band in the y-axis) for the four VIs (NDVI, SAVI, TSAVI, and EVI2).

The behavior of  $\phi_1$ ,  $\psi_1$ , and  $\phi_2$  suggest several dependency relationships. The coefficients  $\psi_1$  and  $\phi_2$  were negative over the entire range of both endmember spectra for all four VIs. In contrast,  $\phi_1$  was both positive and negative. Because  $\phi_1 = 0$  implies no difference between the two estimations of FVC, there is an isoline along which the two estimations become identical. This isoline appears at almost the same location for NDVI, SAVI, and TSAVI (Figures 8(a-c)), whereas only EVI2 showed different behavior in this respect (Figure 8(d)). The coefficient  $\psi_1$  depended mostly on the vegetation endmember spectrum for the cases of SAVI, TSAVI, and EVI2 (Figure 8(f-h)), because the contours were parallel to the y-axis. This implied that  $\psi_1$  mainly represented the influence of the vegetation endmember spectrum in these cases. The behavior of  $\nu$  was similar for all four VIs (Figure 8(m-p)), although the location of the zero contour for EVI2 differed somewhat from the other three cases. Because the sign of the difference ( $h(\hat{\omega}_2)$ ) was identical to the sign of  $\nu$ , this result confirmed that the sign of ( $h(\hat{\omega}_2)$ ) was mostly the same for NDVI, SAVI, and TSAVI (as was shown in Figures 5 and 6).

Finally, the plots of  $\hat{\omega}_{2max}$  and  $h(\hat{\omega}_{2max})$  are shown in Figures 9(a-d) and Figures 9(e-h), respectively. In those figures, LAI (the x-axis) represents the vegetation endmember spectrum, and the soil red reflectance (the y-axis) represents the non-vegetation endmember. These figures clearly showed that  $\hat{\omega}_{2max}$  and the maximum difference  $h(\hat{\omega}_{2max})$  (in the absolute sense) depended on the combination of the

endmember spectra to some extent. Interestingly, both  $\hat{\omega}_{2max}$  and  $h(\hat{\omega}_{2max})$  depended more heavily on the choice of non-vegetation endmember spectrum than on the vegetation endmember spectrum, which implies the presence of soil influence on both variables.

## 5. Discussion

Several types of algorithms have been proposed for the purpose of FVC estimation from remotely sensed reflectance spectra. However, the relationships among the FVC estimates derived from a single spectrum using different algorithms had not been fully clarified. The relationships were thoroughly derived in this study by focusing on a limited set of retrieval algorithms based on an LMM. In the algorithms, both the number of endmembers and the number of spectral bands were limited to two each to simplify and clarify the discussion. A general form of the VIs, represented as the ratio of the linear sum of red and NIR reflectances, were assumed to cover several well-known VIs in a single form.

This study derived expressions for the relationships among the various FVC algorithms in the context of these limitations. The major findings of this study were that the one-to-one relationships between algorithms-2 and -3 depended on the choice of endmember spectra (vegetation and non-vegetation classes). The maximum difference between the estimated FVCs, as well as the FVC value at which the maximum occurred, could be written as a function of only one variable,  $\nu$ , which was determined by the endmember spectra. The dependencies were demonstrated and validated numerically using a canopy RT model with a general soil line.

The applicability of the results and findings of this study are mostly restricted by the assumptions imposed on the retrieval algorithms. The analytical relationships were derived only for techniques based on two endmembers and two bands with a VI expressed in the general form. Further investigations would be required to extend this discussion to the analysis of hyperspectral data with constraints represented in a rather complex form. Nevertheless, the fundamental aspects of the derived relationships form a theoretical basis for similar investigations. For this reason, this study is expected to contribute to a better understanding of the retrieval algorithms.

## Acknowledgements

This work was supported by JSPS KAKENHI 21510019 (HY).

## References

1. Lu, H.; Raupach, M.R.; McVicar, T.R. *Decomposition of Vegetation Cover into Woody and Herbaceous Components Using AVHRR NDVI Time Series*; Technical Report 35/01, CSIRO Land and Water: Canberra, Australia, 2001.
2. Jiang, Z.; Huete, A.R.; Chen, J.; Chen, Y.; Li, J.; Yan, G.; Zhang, X. Analysis of NDVI and scaled difference vegetation index retrievals of vegetation fraction. *Remote Sens. Environ.* **2006**, *101*, 366–378.
3. Aman, A.; Randriamanantena, H.P.; Podaire, A.; Frouin, R. Upscale integration of normalized difference vegetation index: The problem of spatial heterogeneity. *IEEE Trans. Geosci. Remote Sens.* **1992**, *30*, 326–338.

4. Jimenéz-Muñoz, J.C.; Sobrino, J.A.; Plaza, A.; Guanter, L.; Moreno, J.; Martinez, P. Comparison between fractional vegetation cover retrievals from vegetation indices and spectral mixture analysis: Case study of PROBA/CHRIS data over an agricultural area. *Sensors* **2009**, *9*, 768–793.
5. Song, C. Spectral mixture analysis for subpixel vegetation fractions in the urban environment: How to incorporate endmember variability? *Remote Sens. Environ.* **2005**, *95*, 248–263.
6. Asner, G.P. Biophysical and biochemical sources of variability in canopy reflectance. *Remote Sens. Environ.* **1998**, *64*, 234–253.
7. Gutman, G.; Ignatov, A. The derivation of the green vegetation fraction from NOAA/AVHRR data for use in numerical weather prediction models. *Int. J. Remote Sens.* **1998**, *19*, 1533–1543.
8. Lobell, D.B.; Asner, G.P.; Law, B.E.; Treuhaft, R.N. Subpixel canopy cover estimation of coniferous forests in Oregon using SWIR imaging spectrometry. *J. Geophys. Res.* **2001**, *106*, 5151–5160.
9. Lu, D.; Moran, E.; Batistella, M. Linear mixture model applied to Amazonian vegetation classification. *Remote Sens. Environ.* **2003**, *87*, 456–469.
10. Braswell, B.H.; Hagen, S.C.; Frohling, S.E.; Salas, W.A. A multivariable approach for mapping sub-pixel land cover distributions using MISR and MODIS: Application in the Brazilian Amazon region. *Remote Sens. Environ.* **2003**, *87*, 243–256.
11. Weng, Q.; Lu, D.; Schubring, J. Estimation of land surface temperature-vegetation abundance relationship for urban heat island studies. *Remote Sens. Environ.* **2004**, *89*, 467–483.
12. Weng, Q.; Lu, D. A sub-pixel analysis of urbanization effect on land surface temperature and its interplay with impervious surface and vegetation coverage in Indianapolis, United States. *Int. J. Appl. Earth Obs. Geoinf.* **2008**, *10*, 68–83.
13. Shimabukuro, Y.E.; Smith, J.A. The least-squares mixing models to generate fraction images derived from remote sensing multispectral data. *IEEE Trans. Geosci. Remote Sens.* **1991**, *29*, 16–20.
14. Xiao, J.; Moody, A. A comparison of methods for estimating fractional green vegetation cover within a desert-to-upland transition zone in central New Mexico, USA. *Remote Sens. Environ.* **2005**, *98*, 237–250.
15. Jasinski, M.F.; Eagleson, P.S. Estimation of subpixel vegetation cover using red-infrared scattergrams. *IEEE Trans. Geosci. Remote Sens.* **1990**, *28*, 253–267.
16. Jasinski, M.F. Estimation of subpixel vegetation density of natural regions using satellite multispectral imagery. *IEEE Trans. Geosci. Remote Sens.* **1996**, *34*, 804–813.
17. Huemmrich, K.F. The GeoSail model: A simple addition to the SAIL model to describe discontinuous canopy reflectance. *Remote Sens. Environ.* **2001**, *75*, 423–431.
18. Carpenter, G.A.; Gopal, S.; Macomber, S.; Martens, S.; Woodcock, C.E. A neural network method for mixture estimation for vegetation mapping. *Remote Sens. Environ.* **1999**, *70*, 138–152.
19. Guilfoyle, K.J.; Althouse, M.L.; Chang, C.-I. A quantitative and comparative analysis of linear and nonlinear spectral mixture models using radial basis function neural networks. *IEEE Trans. Geosci. Remote Sens.* **2001**, *39*, 2314–2318.
20. Adams, J.B.; Smith, M.O.; Johnson, P.E. Spectral mixture modeling: a new analysis of rock and soil types at the Viking Lander 1 site. *J. Geophys. Res.* **1986**, *91*, 8098–8112.

21. Settle, J.J.; Drake, N.A. Linear mixing and the estimation of ground cover proportions. *Int. J. Remote Sens.* **1993**, *14*, 1159–1177.
22. Foody, G.M.; Cox, D.P. Sub-pixel land cover composition estimation using a linear mixture model and fuzzy membership functions. *Int. J. Remote Sens.* **1994**, *15*, 619–631.
23. Ichoku, C.; Karnieli, A. A review of mixture modeling techniques for sub-pixel land cover estimation. *Remote Sens. Rev.* **1996**, *13*, 161–186.
24. García-Haro, F.J.; Gilbert, M.A.; Meliá, J. Linear spectral mixture modelling to estimate vegetation amount from optical spectral data. *Int. J. Remote Sens.* **1996**, *17*, 3373–3400.
25. Zeng, X.; Dickinson, R.E.; Walker, A.; Shaikh, M.; Defries, R.S.; Qi, J. Derivation and evaluation of global 1-km fractional vegetation cover data for land modeling. *J. Appl. Meteorol.* **2000**, *39*, 826–839.
26. Hirano, Y.; Yasuoka, Y.; Shibasaki, R. Pragmatic approach for estimation of vegetation cover ratio in urban area using NDVI. *J. Jpn. Soc. Remote Sens. (in Japanese with English abstract)* **2002**, *22*, 163–174.
27. Haertel, V.F.; Shimabukuro, Y.E. Spectral linear mixing model in low spatial resolution image data. *IEEE Trans. Geosci. Remote Sens.* **2005**, *43*, 2555–2562.
28. Pu, R.; Gong, P.; Michishita, R.; Sasagawa, T. Spectral mixture analysis for mapping abundance of urban surface components from the Terra/ASTER data. *Remote Sens. Environ.* **2008**, *112*, 939–954.
29. Hestir, E.L.; Khanna, S.; Andrew, M.E.; Santos, M.J.; Viers, J.H.; Greenberg, J.A.; Rajapakse, S.S.; Ustin, S.L. Identification of invasive vegetation using hyperspectral remote sensing in the California Delta ecosystem. *Remote Sens. Environ.* **2008**, *112*, 4034–4047.
30. Zhang, J.; Rivard, B.; Rogge, D.M. The successive projection algorithm (SPA), an algorithm with a spatial constraint for the automatic search of endmembers in hyperspectral Data. *Sensors* **2008**, *8*, 1321–1342.
31. Chen, J.; Jia, X.; Yang, W.; Matsushita, B. Generalization of subpixel analysis for hyperspectral data with flexibility in spectral similarity measures. *IEEE Trans. Geosci. Remote Sens.* **2009**, *47*, 2165–2171.
32. Small, C. Estimation of urban vegetation abundance by spectral mixture analysis. *Int. J. Remote Sens.* **2001**, *22*, 1305–1334.
33. Chang, C.I.; Ren, H.; Chang, C.C.; D’Amico, F.; Jensen, J.O. Estimation of subpixel target size for remotely sensed imagery. *IEEE Trans. Geosci. Remote Sens.* **2004**, *42*, 1309–1320.
34. Van de Voorde, T.; Vlaeminck, J.; Canters, F. Comparing different approaches for mapping urban vegetation cover from landsat ETM+ data: A case study on Brussels. *Sensors* **2008**, *8*, 3880–3902.
35. Cavalli, R.M.; Pascucci, S.; Pignatti, S. Optimal spectral domain selection for maximizing archaeological signatures: Italy case studies. *Sensors* **2009**, *9*, 1754–1767.
36. Wittich, K.P.; Hausing, O. Area-averaged vegetative cover fraction estimated from satellite data. *Int. J. Biometeorol.* **1995**, *38*, 209–215.
37. Carlson, T.N.; Ripley, D.A. On the relation between NDVI, fractional vegetation cover, and leaf area index. *Remote Sens. Environ.* **1997**, *62*, 241–252.

38. Carlson, T.N.; Arthur, S.T. The impact of land use-land cover changes due to urbanization on surface microclimate and hydrology: A satellite perspective. *Global Planet. Change* **2000**, *25*, 49–65.
39. Zhang, X.; Yan, G.; Li, Q.; Li, Z.L.; Wan, H.; Guo, Z. Evaluating the fraction of vegetation cover based on NDVI spatial scale correction model. *Int. J. Remote Sens.* **2006**, *27*, 5359–5372.
40. Rouse, J.W.; Haas, R.H.; Schell, J.A.; Deering, D.W. Monitoring vegetation systems in the great plains with ERTS. In *Proceedings of 3rd ERTS Symposium*, Washington, DC, USA, December 1974; NASA SP-351, pp. 309–317.
41. Tucker, C.J. Red and photographic infrared linear combinations for monitoring vegetation. *Remote Sens. Environ.* **1979**, *8*, 127–150.
42. Richardson, A.J.; Wiegand, C.L. Distinguishing vegetation from soil background information (by gray mapping of Landsat MSS data). *Photogramm. Eng. Remote Sens.* **1977**, *43*, 1541–1552.
43. Huete, A.R. A soil-adjusted vegetation index (SAVI). *Remote Sens. Environ.* **1988**, *25*, 295–309.
44. Baret, F.; Guyot, G. Potentials and limits of vegetation indices for LAI and APAR assessment. *Remote Sens. Environ.* **1991**, *35*, 161–173.
45. Baret, F.; Guyot, G.; Major, D. TSAVI: A vegetation index which minimizes soil brightness effects on LAI and APAR estimation. In *Proceedings of IGARSS 89, 12th Canadian Symposium on Remote Sensing*, Vancouver, Canada, 1989; Vol. 3, pp. 1355–1358.
46. Jiang, Z.; Huete, A.R.; Didan, K.; Miura, T. Development of a two-band enhanced vegetation index without a blue band. *Remote Sens. Environ.* **2008**, *112*, 3833–3845.
47. Liu, H.Q.; Huete, A.R. A feedback based modification of the NDVI to minimize canopy background and atmospheric noise. *IEEE Trans. Geosci. Remote Sens.* **1995**, *33*, 457–465.
48. Huete, A.R.; Post, D.F.; Jackson, R.D. Soil spectral effects on 4-space vegetation discrimination. *Remote Sens. Environ.* **1984**, *15*, 155–165.

© 2010 by the authors; licensee MDPI, Basel, Switzerland. This article is an Open Access article distributed under the terms and conditions of the Creative Commons Attribution license (<http://creativecommons.org/licenses/by/3.0/>).